PNAS RESEARCH ARTICLE | BIOPHYSICS AND COMPUTATIONAL BIOLOGY

Elevator mechanism dynamics in a sodium-coupled dicarboxylate transporter

Colin D. Kinz-Thompson[a,1], Maria Louisa Lopez-Redondo[b,2], Christopher Mulligan[c], David B. Sauer[b,3], Jennifer J. Marden[b], Jinmei Song[b], Emad Tajkhorshid[d], John F. Hunt[e], David L. Stokes[b], Joseph A. Mindell[f,4], Da-Neng Wang[b,4], and Ruben L. Gonzalez Jr.[a,g,4]

Affiliations are included on p. 11.

Edited by Ahmet Yildiz, University of California Berkeley Biophysics Group, Berkeley, CA; received January 11, 2025; accepted December 4, 2025 by Editorial Board Member James H. Hurley

VcINDY, the sodium-dependent dicarboxylate transporter from *Vibrio cholerae*, is responsible for C_4-carboxylate uptake into cells. The molecular mechanism of how VcINDY physically moves substrates across the membrane, and does so in an energetically efficient manner, is unclear. Here, we use single-molecule fluorescence resonance energy transfer experiments to directly observe the individual mechanistic steps that VcINDY takes to translocate substrates across a lipid bilayer, and then test key predictions of transport cycle mechanistic models. Our data provide the first direct, dynamic evidence that VcINDY undergoes stochastic, elevator-type conformational motions that enable substrate translocation. The dynamics of these elevator motions are approximately an order of magnitude faster than the turnover rate for substrate transport, demonstrating that VcINDY undergoes multiple rounds of substrate translocation before a productive transport cycle is completed. Furthermore, the two protomers of the VcINDY homodimer undergo the substrate translocation motions in a noncooperative manner, and thus likely engage in independent transport reactions. The relative substrate independence of those motions supports the notion that the VcINDY transport cycle maintains strict cosubstrate coupling by a mechanism other than translocation inhibition. Thermodynamic modeling provides insight into how a cooperative binding mechanism is one such generalized approach to optimizing transport for many secondary active transporters.

secondary active transporter | translocation mechanism | thermodynamic cycle efficiency | single-molecule fluorescence resonance energy transfer

Secondary active transporters are transmembrane proteins that harvest free energy from electrochemical gradients to drive the movement of substrates across a membrane (Fig. 1) (1). In the absence of a free energy source, these transporters move substrates back and forth across the membrane without creating a net change in substrate concentration (2). Net transport occurs because the transporter can dissipate the electrochemical gradient of a "driving" substrate to harvest free energy, and then couple that free energy to the "uphill" movement of a "driven" substrate across the membrane (3). The mechanistic details of this coupling are governed by the transport cycle, which describes how the transporter binds its substrates, translocates them across the membrane, releases them, and resets itself for the next round (Fig. 1*B*). While the specific details of the transport cycle and how it is achieved on a molecular level are unique to each transporter or transporter family, the active use of free energy suggests that transport cycles must maintain strict substrate coupling to minimize energetically wasteful "slippage cycles" (c.f., Fig. 1*B*) in which driving substrates are transported without driving the translocation of the driven substrate (1).

While all secondary active transporters work by facilitating a general, dynamic equilibrium (e.g., $mA_{\text{outside}} + nB_{\text{outside}} \rightleftharpoons mA_{\text{inside}} + nB_{\text{inside}}$, where A and B are cosubstrates with stoichiometries m and n), the molecular details of how this chemical reaction maps onto the transport cycle are determined by the conformational dynamics of the transporter. According to the alternating access hypothesis, secondary active transporters must undergo a reversible conformational transition between at least two distinct conformational states: one with the substrate-binding pocket in a state that is "outward-facing" with respect to the membrane (C_o), and one in an "inward-facing" state (C_i) (2). While there are many possible structural implementations of alternating access, including the so-called "rocker-switch," "rocking-bundle," and "elevator" transport mechanisms (4), at least two distinct conformational transitions between C_i and C_o must occur in a complete transport cycle (c.f., Fig. 1*B*). Here, we investigate the role of such conformational dynamics in the

Significance

Transporter proteins use energy to move molecular materials into and out of cells. To be efficient, the transporter motions responsible for moving the molecules must be tightly choreographed to avoid wasting energy without transporting anything. By measuring the motions and kinetics of a prototypical transporter (VcINDY) at the single-molecule level, this study finds the first evidence that transporters like VcINDY achieve efficient transport by coordinating constantly dynamic, "elevator-type" motions while sitting in the cellular membrane. The efficiency of these surprisingly dynamic transporters is then revealed by thermodynamic modeling, which explains the molecular basis behind how highly cooperative, substrate-binding reactions may have evolved as the optimal strategy for maximizing transporter efficiency.

Preprint Servers: bioRxiv; ID: 490196.

This article is a PNAS Direct Submission. A.Y. is a guest editor invited by the Editorial Board.

[1] Present address: Department of Chemistry, Rutgers University-Newark, Newark, NJ 07102.

[2] Present address: Instituto de Biomedicina de Valencia, Consejo Superior de Investigaciones Científicas, Valencia 46010, Spain.

[3] Present address: Nuffield Department of Medicine, Centre for Medicines Discovery, University of Oxford, Oxford OX1 3QU, United Kingdom.

[4] To whom correspondence may be addressed. Email: mindellj@ninds.nih.gov, da-neng.wang@med.nyu.edu, or rlg2118@columbia.edu.

This article contains supporting information online at https://www.pnas.org/lookup/suppl/doi:10.1073/pnas.2500723123/-/DCSupplemental.

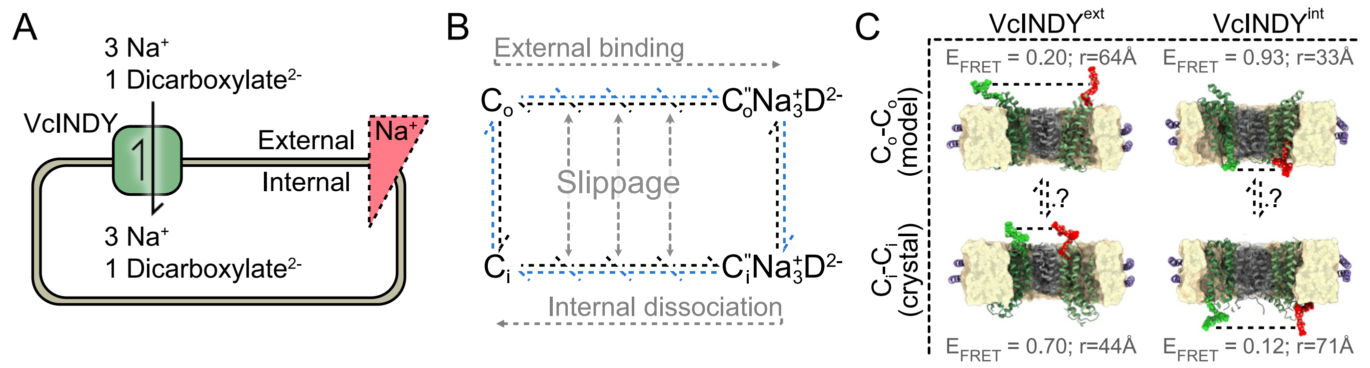

Fig. 1. VcINDY transport cycle. (*A*) Diagram of VcINDY dimer (green) reversibly transporting sodium ions (Na^+) and dicarboxylate substrate (D^{2-}) into and out of a cell with a stoichiometry of 3:1; an inward-facing Na^+ electrochemical gradient provides the free energy for vectorial transport. (*B*) Minimal mechanistic model of VcINDY transport cycle. Outward- and inward-facing conformations of the VcINDY homodimer (C_o, and C_i, respectively) bind Na^+ and D^{2-} in an unknown order along the horizontal transitions; double-prime signifies both cosubstrates are bound. VcINDY protomer conformational motions along the vertical transitions are involved in substrate translocation. At least one closed transport cycle, such as shown here in the clockwise direction in blue, is required for vectorial transport. Slippage reactions occur when an incomplete set of cosubstrates is moved across the membrane. (*C*) Cartoon diagram of smFRET pairs designed to report on the VcINDY translocation reaction for VcINDY^{ext} (*Left*; G211) and VcINDY^{int} (*Right*; S436). The distance between each labeling position, *r*, was determined from the C_α-C_α distance, and was measured for a C_o, substrate-bound repeat-swap model (C_o-C_o, PMDB: PM0080216), and a substrate-bound, C_i X-ray crystallography structure (C_i-C_i, PDB: 5UL9). E_{FRET} was estimated using R_0 = 51 Å. Scaffold domains are shown in gray, and transport domains are shown in green.

transport cycle of the prototypical sodium-dependent divalent anion transporter from mesophilic *Vibrio cholerae*, VcINDY, and elucidate how they are tuned to enable efficient transport and minimize slippage.

VcINDY is a well-characterized member of the divalent anion/sodium symporter (DASS) class of secondary active transporters, which extends across all kingdoms of life. In mammals, it is represented by the solute carrier 13 (SLC13) gene family, which includes members that transport di- and trivalent anions, including sulfate, citrate, and succinate (5, 6). Within this family, the SLC13A5 citrate transporter, NaCT, has significant metabolic and neurologic health importance for humans, and mutations in NaCT can cause epilepsy in children (reviewed in ref. 7). Like NaCT, VcINDY is a Na^+-driven carboxylate transporter, but VcINDY is primarily a succinate transporter with an electrogenic transport cycle stoichiometry of three Na^+ ions per succinate (Fig. 1*A*) (8, 9). Over the past decade, extensive in vitro biochemical characterization (8–12), and deep structural insight from X-ray crystallography, cryoelectron microscopy (cryo-EM), and computational studies (10, 13–16), have made VcINDY into the prototypical transporter for understanding the mechanistic details of transport in the DASS family.

While the biochemical and structural studies published to-date do not yield a description of the molecular mechanism for the complete VcINDY transport cycle, recent combinations of computational modeling, biochemical, and structural analysis have provided insight (10, 17). Structural studies have revealed VcINDY is a homodimeric membrane protein with twofold rotational symmetry; however, in all these studies, VcINDY was only observed in a single C_i conformational state in which the substrate-binding pockets of both protomers are accessible only from the cytosolic side (i.e., the global homodimer conformation is C_i-C_i) (13, 14, 16, 17). Computational and crosslinking studies suggest that VcINDY functions using an elevator mechanism, with a large translocation of the "transport" domain that carries substrates from one side of the membrane to the other, and a relatively stationary "scaffold" domain that harbors the dimerization interface (10). This model is supported by recent structural work revealing a C_o state for LaINDY, a close homolog from *Lactobacillus acidophilus* (17), and a mixed C_o-C_i state for the human NaDC3, a related SLC13 family member (18). While these static, structural lines of evidence are consistent only with an elevator mechanism, and not with rocker-switch or rocking-bundle mechanisms, there has been no experimental observation of a transition between these C_o and C_i states and thus no direct dynamic evidence that they are responsible for achieving alternating access during transport. Comprehensive validation of the elevator model requires confirming the proposed elevator motions, connecting them to the transport cycle, and understanding how those conformational dynamics enable VcINDY to achieve tight cosubstrate coupling between Na^+ and succinate to minimize energetically costly slippage of substrates across the membrane (Fig. 1*B*).

In this work, using single-molecule fluorescence resonance energy transfer (smFRET) microscopy, we aimed to directly observe the global conformational dynamics of homodimeric VcINDY in a lipid bilayer membrane, allowing us to characterize the structural and kinetic details of its transport cycle. To achieve this, we designed two complementary VcINDY constructs for smFRET experiments. Each smFRET construct contained a FRET donor- and acceptor fluorophore pair engineered at residue positions such that the resulting donor–acceptor distance-dependent FRET efficiency (E_{FRET}) would report on the conformational dynamics responsible for substrate translocation (Fig. 1*C*). These smFRET constructs can therefore be used to directly observe the motions that VcINDY undergoes to achieve alternating access (Fig. 1*B*). In performing smFRET experiments with these constructs, we obtained direct experimental evidence that i) global conformational dynamics of VcINDY during the transport cycle are consistent with the elevator model of transport, ii) the individual protomers of homodimeric VcINDY exhibit minimal cooperativity, and iii) VcINDY minimizes slippage using a mechanism in which cosubstrate binding is highly cooperative. These findings provide the first comprehensive description of the molecular underpinnings of the VcINDY transport cycle, and, by extension, deep insight into the transport cycle of all DASS transporters.

Results

smFRET Constructs Reporting on Substrate Translocation Were Designed, Constructed, and Functionally Validated. In order to directly monitor the VcINDY conformational dynamics relevant to the transport cycle (Fig. 1*B*), we designed two smFRET constructs based on the assumption that substrate translocation in VcINDY involves a large-scale conformational change between the C_o-C_o and the C_i-C_i conformations (c.f., Fig. 1*C*) (10, 13, 14, 17). Taking advantage of the homodimeric nature of VcINDY, one construct was designed to contain a FRET donor- and acceptor fluorophore pair on the external, periplasmic face of the transport domains of VcINDY whereas the other construct was designed to contain them on the internal, cytosolic face. These complementary designs comprise a "multiperspective" approach with an internal self-consistency where any global conformational motions of the VcINDY homodimer occurring during the transport cycle (e.g., an elevator motion) can be detected on both the external and internal sides of the protein.

To design these "external" and "internal" smFRET constructs, we identified solvent-exposed, extramembranous residues in the transport domain with optimal distances between the two equivalent positions across the homodimer (Fig. 1*C*). Specifically, residues were chosen such that the distance would undergo a significant change upon a transition between the structurally defined C_i-C_i and the computationally predicted C_o-C_o states (10, 13, 14, 17). In an optimized smFRET experiment, the corresponding change in the distance-dependent E_{FRET} will utilize the full dynamic range of E_{FRET} from zero to one. To achieve this, we sought residues that moved from separations of less than the half-maximum E_{FRET} of the donor–acceptor pair (R_0) to more than the R_0, or vice versa. We used Alexa Fluor 555 as our donor and Alexa Fluor 647 as our acceptor, with an $R_0 \sim 51$ Å (19). Given these considerations, we chose Gly211, located on the extracellular face of the transport domain as our external site, with a predicted E_{FRET} change from ~0.20 to ~0.93 upon a transition from the C_o-C_o to the C_i-C_i state (Fig. 1*C*). Likewise, we chose Ser436, located on the cytoplasmic face of the transport domain as our internal site, with a predicted E_{FRET} change from ~0.70 and ~0.12 upon transition from the C_o-C_o to the C_i-C_i state. Single VcINDY homodimer E_{FRET} *versus* time trajectories (i.e., E_{FRET} trajectories) recorded using the external and internal smFRET constructs should then report upon the same set of global VcINDY conformational dynamics involved in substrate translocation but from different perspectives.

Biochemically active variants of the two VcINDY smFRET constructs designed above were created, overexpressed, purified, and labeled with donor and acceptor fluorophores to generate the externally and internally labeled smFRET constructs (VcINDY^{ext} and VcINDY^{int}, respectively) (*Materials and Methods*) (*SI Appendix*, Fig. S1). Both VcINDY^{ext} and VcINDY^{int} were able to catalyze substrate translocation in liposomes, and exhibited transport activities that were only threefold reduced relative to wildtype VcINDY and were similar to the activity of the unlabeled cysteine-containing mutants (*SI Appendix*, Fig. S2). Importantly, these single-cysteine mutants were created in the cysteine-less background of a previously reported construct that can achieve alternating access and exhibits a transport rate that is only reduced by fivefold relative to the wildtype (10, 11). To investigate the conformational dynamics of VcINDY in a membrane, we reconstituted VcINDY^{ext} and VcINDY^{int} into lipid bilayer nanodiscs (Fig. 2) (20). Nanodisc-based experimental conditions are ideal for interrogating the C_o to C_i transition at equilibrium, since both sides of the membrane are exposed to identical solutions. Furthermore, the nanodiscs used here have a diameter of ~108 Å (21), which helped establish single-molecule resolution by ensuring that only a single VcINDY dimer could occupy each nanodisc. After chromatographic purification, these nanodiscs appeared well dispersed when imaged using negative stain electron microscopy (*SI Appendix*, Fig. S3).

smFRET experiments were performed using a widefield, total internal reflection fluorescence (TIRF) microscope to record the fluorescence intensity emitted from individual, immobilized VcINDY-containing nanodiscs (Fig. 2). The corresponding E_{FRET} trajectory for each molecule was then calculated using $E_{FRET} = I_{acceptor}/(I_{donor} + I_{acceptor})$, where I_x is the observed intensity of either the donor or the acceptor fluorophore. Along with the chromatographic purification used in nanodisc reconstitution, the selection criteria for E_{FRET} trajectory (*Materials and Methods*), ensured that each E_{FRET} trajectory originated from a single VcINDY dimer (*SI Appendix*, Fig. S1).

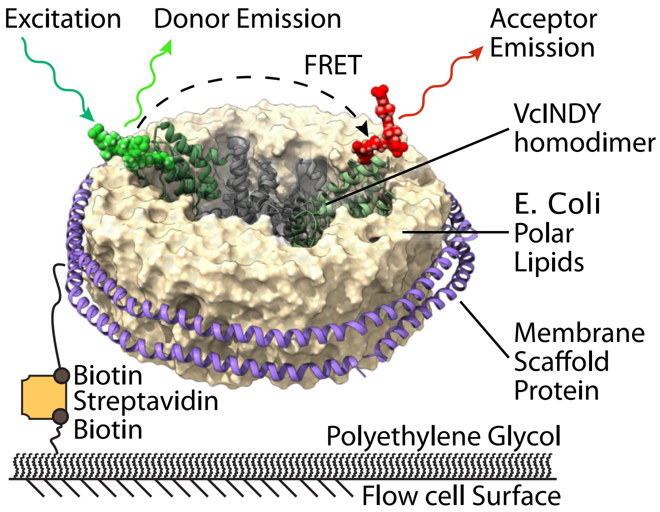

Fig. 2. Schematic diagram of nanodisc-embedded VcINDY homodimer construct. Single cysteine mutant VcINDY labeled with a 1:1 ratio of donor and acceptor fluorophores is mixed with biotinylated membrane scaffold protein (MSP) and *E. coli* polar lipids to make nanodisc-embedded dimers. VcINDY containing nanodiscs are then tethered to a flow cell surface via a biotin–streptavidin–biotin bridge, and imaged using TIRF microscopy. The scaffold domains are shown in gray, and transport domains are shown in green.

E_{FRET} States Consistent with Elevator-Type Motions Are Stochastically Sampled during VcINDY Substrate Translocation. To characterize the conformational dynamics of VcINDY during the transport cycle (Fig. 1*B*), we performed equilibrium smFRET experiments using VcINDY^{ext} or VcINDY^{int} in which the buffer contained saturating concentrations of both Na$^+$ and succinate cosubstrates (Buffer HS: High Na$^+$ with Succinate). The conformational dynamics that occur under these conditions are the same as those involved in vectorial transport—even in the absence of a chemical free energy driving force (1). Thus, by saturating the VcINDY smFRET constructs with both cosubstrates, we expected to record E_{FRET} trajectories that report on the equilibrium conformational dynamics of the substrate translocation reaction between a substrate-bound C_o state and a substrate-bound C_i state (C_o" and C_i" in Fig. 1*B*), which we hypothesized resemble the C_o-C_o and C_i-C_i conformations, respectively (Fig. 1*C*).

In the presence of both Na$^+$ and succinate, the E_{FRET} trajectories originating from individual VcINDY^{ext} or VcINDY^{int} dimers exhibited stochastic, instantaneous jumps between transiently stable states characterized by distinct E_{FRET} values (i.e., E_{FRET} states) (Fig. 3). Visual inspection showed that individual E_{FRET} trajectories could visit many distinct E_{FRET} states (e.g., Fig. 3, *Lower*), and the same E_{FRET} states were often revisited within a single E_{FRET} trajectory. Most E_{FRET} trajectories, however, exhibited just a few jumps to a small number of distinct E_{FRET} states before relatively rapid photobleaching of the donor and/or acceptor fluorophores prematurely ended our ability to measure E_{FRET}. Qualitatively, the lifetimes of these E_{FRET} states were generally several seconds. Notably, the E_{FRET} states that are observed across the entire population of VcINDY^{ext} or VcINDY^{int} E_{FRET} trajectories (Figs. 3 and 4) are consistent with the range of predicted E_{FRET} values for large, elevator-type conformational transitions

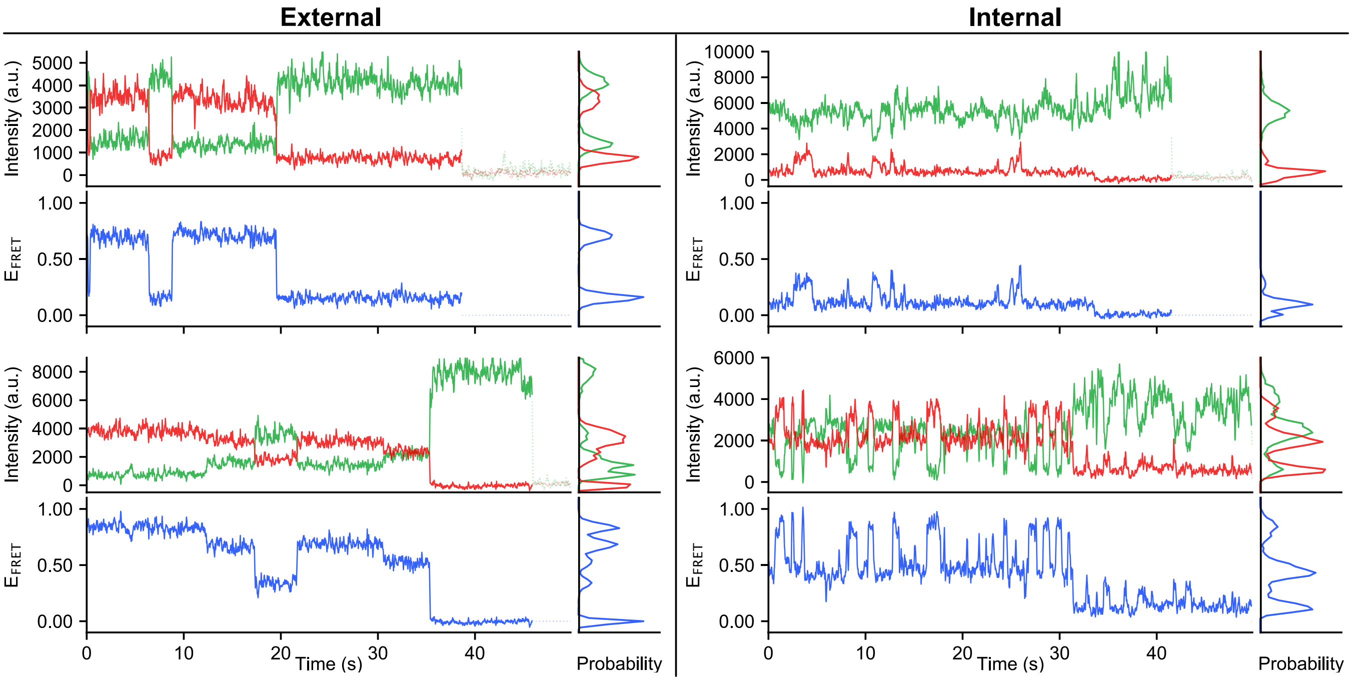

Fig. 3. Equilibrium smFRET from VcINDY^{ext} (*Left*) and VcINDY^{int} (*Right*) in the presence of sodium and succinate (buffer HS). Example donor (green) and acceptor (red) fluorescence intensity trajectories, with corresponding E_{FRET} trajectories (blue). Several trajectories shown include donor fluorescence intensity after the acceptor fluorophore has photobleached, but this was removed prior to further analysis.

between the C_o-C_o and C_i-C_i conformations using the symmetric, donor–acceptor pairs engineered into both VcINDY^{ext} and VcINDY^{int} (Fig. 1*C*).

VcINDY Reversibly Populates C_o-C_o, C_i-C_i, and Mixed C_o-C_i Conformational States during Substrate Translocation. Assuming transmembrane substrate translocation requires transitions solely between the C_o-C_o and C_i-C_i conformations of VcINDY, we predicted that E_{FRET} trajectories from both VcINDY^{ext} and VcINDY^{int} should exhibit transitions between at least two E_{FRET} states (Fig. 1*C*). Instead, we observed transitions that were inconsistent with just two E_{FRET} states for both constructs (Figs. 3 and 4). Change-point modeling to generate transition density plots (TDP) (*SI Appendix*, Figs. S4 and S5) revealed that the individual, stable E_{FRET} states are heterogeneous and broadly distributed, and that the transitions between them form characteristic banded patterns in the TDPs indicative of one-protomer-at-a-time conformational changes. The simplest interpretation of this observation is that the two protomers within a VcINDY dimer can independently undergo elevator-type conformational transitions. If that were the case, VcINDY dimers could then sample "mixed," asymmetric dimer conformations (e.g., C_o-C_i). Many structural studies support the existence of such asymmetric dimers as NaDC3—a related DASS transporter from the human SLC13 family—has been observed to populate a C_o-C_i conformation (18), and so have other dimeric secondary active transporters with the same fold as VcINDY (22–24). Moreover, succinate transport by VcINDY occurs with a Hill coefficient of 0.88 ± 0.13, rather than two, suggesting that the VcINDY protomers function independently of one another (8). To determine whether our smFRET data are consistent with such an interpretation, we used a state-of-the-art smFRET data analysis algorithm implemented in the tMAVEN software package to statistically determine the most parsimonious kinetic model that captures the broad range of E_{FRET} states and transition dynamics observed across the entire set of E_{FRET} trajectories obtained from each construct, VcINDY^{ext} and VcINDY^{int} (25) (*Materials and Methods*) (*SI Appendix*, Figs. S6 and S7). These kinetic models are hidden Markov models (HMMs), which are the standard approach to analyzing smFRET data, and allow for the optimal number of E_{FRET} states to be statistically determined (*Materials and Methods* and *SI Appendix*). The determination of the optimal number of states using an HMM is done by considering both the E_{FRET} values and their dynamics in a Bayesian framework, which provides a rigorous approach for model selection in single-molecule analyses, particularly when accounting for data sparsity and uncertainty (26).

For both VcINDY^{ext} and VcINDY^{int}, the most parsimonious kinetic model that can simultaneously account for the entire set of E_{FRET} trajectories was a three-state model (Fig. 4 and *SI Appendix*, Figs. S8 and S9). Notably, this was also true for smFRET data recorded under the four different combinations of sodium and succinate concentrations we investigated using VcINDY^{int} (discussed below). Because these three states persisted across different smFRET constructs and different sodium and succinate concentrations (Fig. 4 and *SI Appendix*, Figs. S8 and S9), we concluded that our smFRET data primarily report on transitions between three distinct conformations of the VcINDY dimer. Nonetheless, individual E_{FRET} trajectories sampled more than three E_{FRET} states that, given the high signal-to-background ratio of the data, were unambiguously distinct from one another (Fig. 3). This observation tentatively suggests that each of the three states identified in our kinetic model may encompass an ensemble of conformations that are globally similar but exhibit localized structural variations near one or both fluorophore-labeling sites, an effect observed in related transporters such as NaDC3, where rearrangements around the substrate-binding region occur without altering the global conformation (18). Additional experiments will be needed to determine whether the heterogeneity observed in these VcINDY E_{FRET} trajectories reflects genuine conformational substates.

Based on the alternating access principle, we expected that the C_o and C_i conformations of the transport cycle (Fig. 1*B*) should be represented within the three states of our kinetic model (2) (Fig. 4). For VcINDY^{ext}, the state characterized by an average

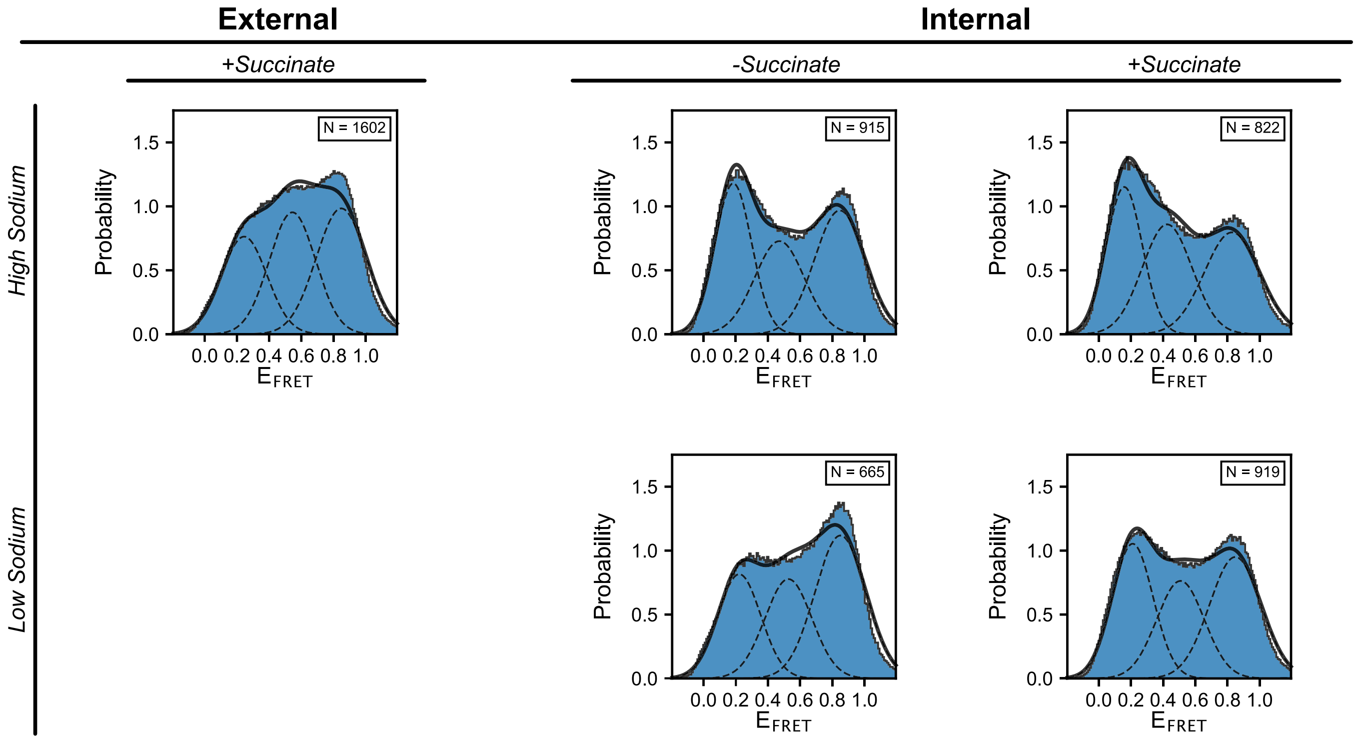

Fig. 4. Substrate dependence of VcINDY E_{FRET} distributions. Histograms of E_{FRET} values from all external (*Left*) and internal (*Right*) smFRET signals recorded with VcINDY^{ext}, and VcINDY^{int}, respectively, in different buffer conditions. *N* refers to the number of individual single-molecule E_{FRET} trajectories contributing to each histogram and used in subsequent analyses. The E_{FRET} data in these histograms were not filtered, and E_{FRET} values corresponding to donor photobleaching have been removed (i.e., the last dwell in an E_{FRET} state of zero). The dashed black curves in each histogram denote the population distributions of the three states that are obtained from kinetic modeling, while the solid black curve denotes the total population distribution from all three states of the kinetic model.

E_{FRET} value of 0.25 is consistent with our prediction of E_{FRET} = 0.20 for the C_o-C_o conformation, and the state characterized by an average E_{FRET} value of 0.85 is consistent with our prediction of E_{FRET} = 0.93 for the C_i-C_i conformation (Fig. 1*C* and *SI Appendix*, Fig. S9). Likewise, for VcINDY^{int}, the state characterized by an average E_{FRET} value of 0.83 is consistent with our prediction of E_{FRET} = 0.70 for the C_o-C_o conformation, and the state characterized by an average E_{FRET} value of 0.16 is consistent with our prediction of E_{FRET} = 0.12 for the C_i-C_i conformation (Fig. 1*C* and *SI Appendix*, Fig. S9). While there is no structural evidence to date that VcINDY uses a different transport mechanism, such as the rocker-switch or rocking-bundle (10, 17, 18), making it impossible to quantitatively speculate, the extent of the transport domain motion would likely be less than the large rigid body motion involved in the elevator mechanism in those cases (4), and therefore they would likely yield smFRET data exhibiting a smaller E_{FRET} range than observed here. Thus, the conformations of VcINDY that are sampled in our smFRET data are broadly consistent with the elevator mechanism suggested by previous structural work and therefore illustrate how stochastic VcINDY conformational changes are coupled to its transport cycle.

There are many effects that could give rise to the small differences we see between our observed and predicted E_{FRET} values ($\Delta E_{FRET} \sim 0.1$). These include i) differences between the C_o-C_o and/or C_i-C_i conformations that nanodisc-embedded VcINDY adopts in our smFRET experiments and the corresponding conformations that are observed in the X-ray, cryo-EM, and computational studies (10, 13, 14, 17); ii) structural perturbations of VcINDY due to fluorophore labeling; iii) unaccounted-for contributions the linkers used to covalently attach the fluorophores to the protein make to the distance between fluorophores; iv) constraints on fluorophore mobility due to interactions with the protein and/or membrane; or even iv) photophysical complications such as "photoblinking" of the fluorophores. Given these effects, along with the uncertainty in which kinetic averaging regime the fluorescence emission occurs for this system (27), we have not attempted to convert the observed, average E_{FRET} values to distances. Nonetheless, given the consistency of our experimental E_{FRET} values with the predicted E_{FRET} values for the C_o-C_o and C_i-C_i conformations, we were able to assign two of the states in our three-state kinetic model to specific VcINDY conformations involved in substrate translocation. Specifically, we assigned the state in our kinetic model that exhibited average E_{FRET} values of 0.25 and 0.83 for VcINDY^{ext} and VcINDY^{int}, respectively, to the C_o-C_o conformation. Likewise, we assigned the state in our kinetic model that exhibited average E_{FRET} values of 0.85 and 0.16 for VcINDY^{ext} and VcINDY^{int}, respectively, to the C_i-C_i conformation. Notably, these assignments are self-consistent in that the most populated VcINDY conformation is the C_i-C_i conformation, regardless of whether it is the VcINDY^{ext} or VcINDY^{int} smFRET data that are analyzed (Fig. 4).

The remaining, unassigned state in our kinetic model can be explained as VcINDY in either a mixed C_o-C_i conformation, or a unique intermediate conformation that is distinct from C_o-C_o and C_i-C_i. Based on biochemical and structural considerations, we favor assigning this state to the more parsimonious, mixed C_o-C_i conformation. The existence of such a conformation is only possible if the protomers of VcINDY operate independently—a possibility that is consistent with the results of previous VcINDY succinate transport kinetic measurements (8). Additionally, the twofold rotational symmetry of the VcINDY dimer renders the C_o-C_i and C_i-C_o conformations structurally degenerate such that they would be expected to correspond to a single E_{FRET} value, which is consistent with our results. In contrast, similar symmetry considerations for VcINDY with a unique intermediate protomer conformation would yield up to six distinct VcINDY dimer conformations in the absence of strict protomer cooperativity or anticooperativity. Finally, computational alignment of the VcINDY scaffold domain of the C_o-C_o and C_i-C_i conformations shows that the donor and acceptor fluorophores in a mixed C_o-C_i conformation would be ~50 Å apart for VcINDY^{ext} and ~59 Å apart for VcINDY^{int}—distances that yield predicted E_{FRET} values of 0.53 and 0.29, respectively (*SI Appendix*, Fig. S10). Given the caveats described above, these predicted E_{FRET} values are in reasonable agreement with the average E_{FRET} values of 0.54 and 0.42 for VcINDY^{ext} and VcINDY^{int}, respectively, that characterize the remaining state of our three-state kinetic model (Fig. 4 and *SI Appendix*, Figs. S8 and S9). Thus, these results suggest that substrate transport is noncooperative between the two protomers in VcINDY.

Regardless of whether the VcINDY^{ext} or VcINDY^{int} constructs are used, our kinetic modeling shows that the elevator motion of a single protomer in the VcINDY dimer occurs at a rate of ~0.4 s^{-1} (i.e., once every ~2.5 s) with no apparent directional dependence. The uncertainty in the HMM-inferred rates is approximately a factor of five, and exclusively due to VcINDY conformational dynamics not directly probed by the smFRET pair rather than HMM "fitting error" (*SI Appendix*, Fig. S11). Notably, direct transitions between C_o-C_o and C_i-C_i where both protomers undergo an apparently simultaneous transition within the temporal resolution of our TIRF microscope were nearly an order of magnitude slower (~0.04 s^{-1}), and therefore much less likely to occur. This suggests that the individual protomers of a VcINDY dimer primarily undergo the translocation reaction in an independent and relatively uncoordinated manner. Overall, in these experiments, the elevator motions of VcINDY responsible for substrate translocation are approximately an order of magnitude faster than the turnover rate for transport measured in bulk biochemical transport experiments of ~0.02 s^{-1} (8). Along with the fact that our smFRET experiments were performed at lower a temperature (21 °C vs. 30 °C), this suggests that VcINDY undergoes multiple rounds of $C_o \rightleftharpoons C_i$ transitions before a productive transport event occurs, and that the rate-limiting step of VcINDY, and possibly DASS family, catalyzed transport may involve simultaneous binding of the substrate and sodium cosubstrate.

VcINDY Exhibits Conformational Dynamics That Are Largely Substrate Independent. The basic mechanistic model of a transport cycle for VcINDY makes several fundamental predictions regarding the conformational dynamics that occur during transport (Fig. 1*B*). Consistent with the alternating access hypothesis (2), VcINDY should be able to switch from a C_o to a C_i conformation in the *apo*, substrate-free state. Also, to preserve substrate coupling, we expect that the partially bound transporter (C_o' and C_i' in Fig. 5) will not undergo outward to inward transitions (and vice versa) to minimize uncoupled slippage of Na^+ or succinate. To test these predictions, we performed additional smFRET experiments using VcINDY^{int} in the absence of both cosubstrates (i.e., in the *apo* condition) (Buffer LX: Low Na^+ with No succinate) as well as in the presence of high concentrations of one cosubstrate, but the absence of the other (i.e., in the only Na^+-bound or the only succinate-bound conditions) (Buffer HX: High Na^+ with No succinate; Buffer LS: Low Na^+ with Succinate). Because of the consistency we observed between VcINDY^{int} and VcINDY^{ext} in buffer HS (Figs. 3 and 4), these substrate dependence experiments were performed using only VcINDY^{int}, which exhibited the best photophysical behavior of the two constructs. Where appropriate, we replaced Na^+ with choline to maintain ionic strength and osmolarity. We note that all of our buffers likely contain trace (i.e., "low") amounts of contaminating Na^+, but at several orders of magnitude lower than the Michaelis constant, K_M, measured for transport (K_m = 41.7 mM) (8).

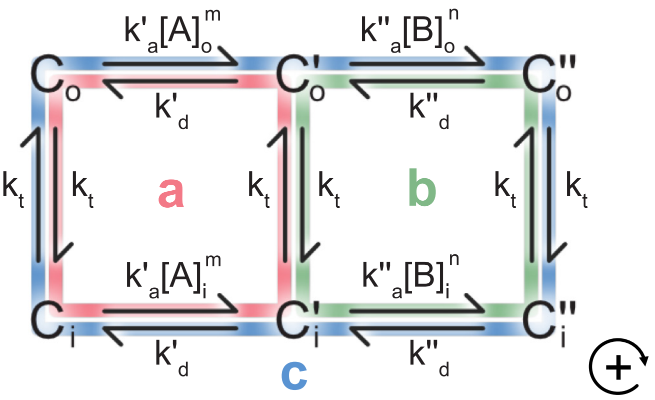

Fig. 5. Free energy transduction model for a secondary active transporter. First-order and pseudo-first-order rate constants for the parsimonious kinetic model discussed in the text are given over each transition. For simplicity, cosubstrate binding has been reduced to a strictly sequential, two-step process with mirror symmetry (1). Substrate A is the first cosubstrate to bind with stoichiometry *m*; cosubstrate B binds second with stoichiometry *n*. Prime signifies the first cosubstrate is bound; double-prime signifies both cosubstrates are bound; C_o and C_i denote the outward and inward-facing conformation of the transporter. k_t is the translocation rate constant, k_a is a second-order association rate constant, and k_d is a dissociation rate constant. Cycles *a* (red) and *b* (green) are responsible for slippage, while cycle *c* (blue) is responsible for transport. The positive direction is defined to be clockwise.

As observed for the smFRET experiments recorded in the presence of high concentrations of both cosubstrates (Buffer HS), the smFRET experiments recorded under all three additional cosubstrate conditions (Buffers LX, HX, and LS) yielded E_{FRET} trajectories that exhibited stochastic, instantaneous jumps between E_{FRET} states spanning a comparably wide range as was seen in Buffer HS (Fig. 4). Computational kinetic analysis showed that the most parsimonious kinetic model that captures the broad range of E_{FRET} states and transition dynamics observed across the entire set of E_{FRET} trajectories recorded under each set of buffer conditions was again a three-state model (*SI Appendix*, Fig. S8). Notably, the E_{FRET} values and transition rate constants obtained under each of these three buffer conditions were similar to each other and to those obtained under the Buffer HS condition (*SI Appendix*, Fig. S9). There were slight differences in the equilibrium population distribution of the three states observed in each buffer condition, and the presence of either substrate somewhat favored the C_i-C_i state (Fig. 4). The kinetics were relatively unchanged, however, with single protomer translocation reactions occurring at a rate of ~0.5 s^{-1} under all buffer conditions tested. Thus, our quantitative kinetic analysis reveals that the conformational motions of VcINDY that are probed along the coordinate between the donor and acceptor fluorophore in VcINDY^{int} are relatively independent of the absence or presence of saturating concentrations of either or both cosubstrates. Although these results conform to our expectation for the *apo* state, the observation of frequent transitions in the E_{FRET} trajectories recorded under the single-cosubstrate conditions was unexpected.

Thermodynamic Modeling Shows That Compensatory Tuning of Cosubstrate Binding and Dissociation Can Minimize Slippage Cycles. In search of an explanation for the surprising kinetics observed under the single-cosubstrate conditions, we next analyzed the thermodynamic efficiency of the VcINDY transport cycle. We modeled the free-energy transduction of a secondary active transporter using Hill's method of cycles (28) to determine how the different molecular processes involved in transport might contribute to slippage. For simplicity, we considered cosubstrate binding as a strictly sequential, two-step process with mirror symmetry (i.e., the same order of cosubstrate binding and dissociation on both faces of the membrane). Specifically, we considered the most parsimonious molecular interpretation of this kinetic scheme for secondary active transport, where i) the rate constants are all first-order or pseudo-first-order, ii) the rate constants are independent of the C_o or C_i state, and iii) the translocation reaction is independent of substrate-binding status (Fig. 5). The resulting, simplified kinetic scheme has three Hill cycles—two of which are involved in slippage (cycles *a* and *b*) and one that is responsible for transport (cycle *c*) (Fig. 5).

We then calculated the thermodynamic efficiency, η, of a transporter with these assumptions (Fig. 5) (28). For a maximally efficient transporter, $\eta \approx 1$ and the transporter tightly couples free energy from the driving to the driven cosubstrate with very little slippage. In that situation, the thermodynamic efficiency is $\eta \propto 1 - \left(\eta_{ac} - \eta_{bc}\right. + \cdots$ with small higher-order terms; here we have assumed A is the driving substrate, but the conclusions discussed below are independent of this. Under our assumptions,

$$\eta_{ac} = \frac{J_a}{J_c} = \left(\frac{[A]_o^m - [A]_i^m}{[A]_o^m[B]_o^n - [A]_i^m[B]_i^n} \quad \left(\frac{2k_t + k''_d}{k''_a} \right) \right),$$

and

$$\eta_{bc} = \frac{J_b}{J_c} = \left(\frac{[B]_o^n - [B]_i^n}{[A]_o^m[B]_o^n - [A]_i^m[B]_i^n} \right.$$
$$\left. \left(\frac{k_t\left([A]_o^m + [A]_i^m\right) + k'_a[A]_o^m[A]_i^m}{k'_d} \right) \right),$$

where J_κ is the cycle flux for cycle κ; concentrations are indicated by square brackets; A and B are the first and second binding cosubstrates with stoichiometries m and n, respectively; the translocation rate constant is k_t, association and dissociation rate constants are k_a and k_d, respectively; and prime and double-prime denote the first and second binding reactions, respectively (Fig. 5). The first terms in these equations show that the relative amount of slippage that a transporter undergoes depends on the instantaneous thermodynamic driving forces via the cosubstrate chemical gradients, while the second terms show that it also depends on the translocation and substrate binding and dissociation reaction kinetics. Thus, the only reliable way nature can optimize this transporter into a highly efficient free energy transducer over a broad range of environmental conditions is to have evolved control over slippage via evolutionary tuning of these rate constants to reduce the total magnitude of η_{ac} and η_{bc}. This suggests that optimal transporters have faced evolutionary pressure to decrease k_t, k'_a and/or k''_d, and to increase k''_a and/or k'_d such that the first binding cosubstrate weakly binds until the second arrives and then both cosubstrates can tightly bind. Unfortunately, tuning these rate constants will also affect the overall transport cycle flux, J_c, and this creates a speed–accuracy tradeoff.

The speed–accuracy tradeoff can, however, be navigated. At the molecular level, the clearest way to reduce slippage is for the binding pocket to stabilize the *apo* and fully bound states (C and C''), by some amount $\Delta G'$ and $\Delta G''$, respectively, and to source all of that energy from a compensatory destabilization of the partially bound conformation, C', by an amount $\Delta G' + \Delta G''$, all without affecting the transition state energy barriers (Fig. 6). This is a conceptually similar idea to the use of substrate-binding energy to stabilize the transition state for enzyme–substrate transition state complementarity (29). In our case, this isoenergetic change decreases k'_a and k''_d while increasing k''_a and k'_d, which reduces slippage and increases the thermodynamic efficiency of the transporter. It also has the effect of increasing the transport cycle flux via ~75% of the terms defining J_c (see *SI Appendix* for the expression for J_c). Given this substantial ability to speed up transport in the complicated expression for J_c, we suspect that these compensatory, isoenergetic binding and dissociation reaction tunings optimally navigate the speed–accuracy tradeoff by simultaneously decreasing the relative fraction of slippage while increasing the total amount of transport. The exact extent of these abilities, however, depends on the instantaneous internal and external cosubstrate concentrations, which can vary significantly across physiologically relevant conditions (*SI Appendix*, Fig. S12) (30). Regardless, this thermodynamic modeling of the free energy transduction efficiency of a secondary active transporter predicts that slippage can be reduced simply by isoenergetic optimization of the energy landscape of the cosubstrate-binding reaction (Fig. 6). In other words, increased cooperativity of cosubstrate binding can itself lead to minimized slippage.

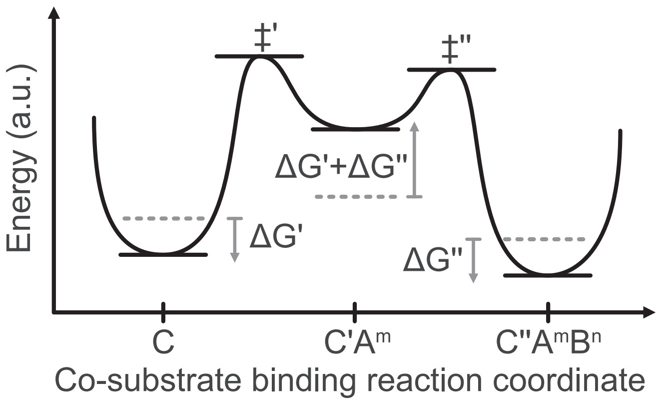

Fig. 6. Schematic of optimized energy landscape for binding cosubstrates A and B. Original energy levels are denoted with dashed lines for apo- (C), partially bound (C'), and fully bound (C'') transporter. Direction of perturbations to energy levels by amounts $\Delta G'$ and $\Delta G''$ are shown with arrows. Relative positioning of unperturbed C, C', and C'', the transition states ‡ ′ and ‡ ′, and the magnitudes of $\Delta G'$ and $\Delta G''$ are arbitrarily chosen to illustrate theoretical principles, and do not reflect energetic parameters measured in this work.

Finally, we also used this thermodynamic modeling-based approach to estimate the occupancy of *apo* VcINDY in our smFRET experiments performed in the presence of only saturating Na^+ (Buffer HX). Specifically, we modeled the reported K_M and V_{max} values for the Na^+ titration and succinate titration experiments that recorded succinate uptake rates in the biochemical proteoliposome-based transport assay data of Mulligan and coworkers (see *SI Appendix* for extended details) (8). This was an underdetermined problem, so we assumed that a single, average rate constant defined several molecular processes: $\langle k \rangle \equiv k_t = k'_d = k''_d$. Markov chain Monte Carlo optimization yielded estimates of $k'_a = 1.5 \times 10^7 M^{-3}s^{-1}$, $k''_a = 7.0 \times 10^8 M^{-1}s^{-1}$, and $\langle k \rangle = 1.05 \times 10^3 s^{-1}$ (*SI Appendix*, Figs. S13 and S14), and reasonably matched the original titration data (*SI Appendix*, Fig. S15). The small mismatch is due to the assumption of a single, average rate constant and the uncertainty in the binding order of the three Na^+ ion- and succinate cosubstrates. Regardless, these estimates are consistent with the biochemical transport data in the context of our kinetic mechanism, so we used them to calculate the steady-state probability of *apo* VcINDY in Buffer HX to be 6.5% (*SI Appendix*). This estimate suggests that even with 100 mM Na^+ in solution, VcINDY still spends a nonnegligible portion of time with an unoccupied binding pocket. Given this result, it is highly likely that the majority of the unexpected elevator motions present in the E_{FRET} trajectories recorded in the presence of only one cosubstrate originate from *apo*, rather than partially bound, VcINDY. This is also in agreement with the charge compensation mechanism proposed for Na^+-substrate coupling in VcINDY (16).

The Dicarboxylate Substrate–Binding Pocket of VcINDY Is Enthalpically Stabilized by Sodium Ions. To obtain atomic-resolution insight into the Na^+ and dicarboxylate substrate–binding reaction for the VcINDY transport cycle, we determined how the conformational state of the VcINDY homodimer is influenced by different dicarboxylate substrates. We therefore separately crystallized detergent-solubilized VcINDY with Na^+ and three different C_4-dicarboxylate substrates (fumarate, malate, and succinate) and solved their structures at 3.09 Å, 3.29 Å, and 3.50 Å, respectively. Regardless of the dicarboxylate substrate identity, VcINDY adopted the same C_i-C_i state in all three of these structures. Similar to what was seen in the previous structure of the C_i-C_i state (13, 14, 16, 17), the binding pocket of the dicarboxylate substrate in all three of these structures was partially comprised of two hairpin loops that coordinated distinct Na^+ ions, Na1 and Na2 (Fig. 7 and *SI Appendix*, Fig. S16). Given this binding geometry, it is possible that tight binding of both cosubstrates requires stabilization of these hairpin loops and that their local conformational rearrangements gate binding and/or dissociation of the cosubstrates.

Discussion

The VcINDY Transport Domain Undergoes Elevator Motions to Enable Alternating Access. The ubiquitous presence in our experiments of stochastic, instantaneous transitions between E_{FRET} states consistent with the C_o-C_o and the C_i-C_i conformations is the first direct evidence for the hypothesis that VcINDY uses an elevator transport mechanism to enable alternating access (Fig. 3) (10). Because we directly observed these stochastic, elevator motions in the presence of substrates but absence of an electrochemical gradient (Buffer HS) and also in the absence of any cosubstrates at all (Buffer LX), it is clear that the VcINDY transport domain can translocate the substrate-binding site across the membrane using only thermal energy—as is expected for the conformational motions of a secondary active transporter that are responsible for transport. Moreover, the rate constants for that process are on the order of 10^{-1} s^{-1} (*SI Appendix*, Fig. S9), suggesting that the energy barrier separating the C_o and C_i states along the translocation reaction coordinate is not prohibitively high. Since the VcINDY transport cycle is much slower and occurs with a rate on the order of 10^{-2} s^{-1} (8), it seems that multiple back-and-forth substrate translocation events occur before a productive transport event is completed. This observation is consistent with a model in which a molecular process other than transport domain translocation governs the transport rate (e.g., gating dynamics within the substrate-binding pocket itself).

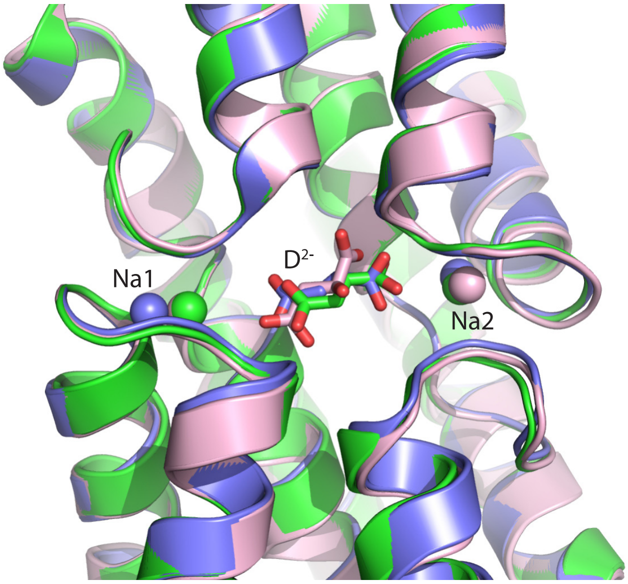

Fig. 7. Overlay of the VcINDY binding pocket viewed from the cytosol. The X-ray crystallography structures of the Na^+- and dicarboxylate (D^{2-})-bound transporter were determined in the presence of three substrates: fumarate (green; PDB ID: 6OKZ), malate (pink; PDB ID: 6OL0), and succinate (blue; PDB ID: 6OL1).

The Conformational Dynamics of VcINDY Protomers Are Noncooperative. The experimental observation of a mixed C_o-C_i conformation for the VcINDY dimer constrains the role that the two protomers can play in the transport cycle. Previously, proteoliposome-based transport experiments determined that VcINDY transports succinate with a Hill coefficient of 0.88 ± 0.13 (8). Given the VcINDY transport stoichiometry of 3:1 Na^+:dicarboxylate (9), this Hill coefficient measurement suggested that the VcINDY transport cycle is noncooperative and that each VcINDY protomer can independently transport succinate. Our observation of a mixed C_o-C_i conformation reveals that VcINDY protomers can undergo independent substrate translocation reactions during vectorial transport, providing a structure-based mechanism for the noncooperative transport cycle of VcINDY. Specifically, since the VcINDY dimer can significantly occupy the C_o-C_i state, the two VcINDY protomers must not undergo a strictly cooperative translocation reaction (i.e., C_o-$C_o \rightleftharpoons C_i$-$C_i$). Furthermore, they must not undergo a strictly anticooperative translocation reaction either (i.e., C_o-$C_i \rightleftharpoons C_i$-$C_o$), because this behavior would preclude occupancy of the C_o-C_o and C_i-C_i conformations observed in our smFRET experiments and structural studies. Therefore, our results provide direct evidence that the VcINDY protomers undergo noncooperative translocation reactions, and that the VcINDY transport cycle itself can be considered to occur independently in each protomer.

In support of this idea, cryo-EM structures of NaDC3, a human SLC13 family homolog of VcINDY, revealed that NaDC3 can exist in the C_o-C_o, C_i-C_i, and mixed C_o-C_i conformations (18). Furthermore, recent structures of CitS, another homodimeric elevator transporter in a different structural family, reveals a CitS dimer with one inward-facing and one outward-facing protomer (22–24), and a recent high-speed atomic force microscopy study of the CitS elevator translocation motion reported that CitS undergoes noncooperative interprotomer conformational dynamics (31). Combined with evidence that Glt_{Ph}, an elevator-type, glutamate transporter that, unlike VcINDY, is from a thermophilic organism, also shows independence between the motions of its three protomers (32–34), these results suggest that such independence may be a general feature of oligomeric elevator transporters (35).

Slippage Cycles Are Avoided without Inhibiting VcINDY Transport Domain Translocation. To avoid wasting the free energy provided by the Na^+ gradient that drives transport of substrates across the membrane, the conformational motions of VcINDY must be coordinated. In particular, VcINDY must minimize slippage cycles in which Na^+ ions are transported across the membrane independent of dicarboxylate (Fig. 1). We had hypothesized that

VcINDY avoids such slippage cycles by inhibiting the substrate-binding pocket translocation reaction (i.e., $C_o \rightleftharpoons C_i$) when substoichiometric amounts of the cosubstrates are bound, and by promoting those motions only when VcINDY is either empty or fully bound. However, the smFRET experiments we recorded under single substrate conditions yielded E_{FRET} trajectories that exhibited no discernable differences in the E_{FRET} states or their rates of transitions, regardless of the presence of relatively high concentrations of either individual cosubstrate in solution (*SI Appendix*, Fig. S9). Given our determination that those observed transitions could reasonably correspond to *apo* VcINDY, it is quite possible that transitions between C_o and C_i in partially bound states are directly suppressed and that we were not able to observe those effects, but our smFRET experiments suggest that VcINDY also uses another, additional mechanism to minimize slippage (Fig. 1*B*).

There are at least two additional mechanisms that VcINDY can use to minimize slippage. One possibility is a secondary conformational change—independent of $C_o \rightleftharpoons C_i$ translocation—to "gate" both binding and release of cosubstrates. For instance, while VcINDY could be able to translocate substrates across the membrane if the $C_o \rightleftharpoons C_i$ transition is not completely inhibited, a slippage cycle cannot be completed without cosubstrate release. Mechanistically, such gating could be achieved with an additional VcINDY conformational equilibrium that is relatively independent of the transport domain translocation reaction $C_o \rightleftharpoons C_i$. Without direct structural insight into such a hypothetical equilibrium, it is attractive to think that it might involve a conformational rearrangement of the binding pocket and, in particular, the hairpin loops (c.f., Fig. 7). In this scenario, the transitions we observe in the smFRET data for partially bound VcINDY would reflect transitions between so-called "occluded" states.

Another possible mechanism to minimize slippage is to ensure that cosubstrate binding is extremely cooperative, such that stable binding requires both cosubstrates to be present. In our smFRET experiments performed in Buffers HX and LS, this mechanism would manifest as transitions in the E_{FRET} trajectories that predominately correspond to transport domain translocation of *apo* VcINDY. This alternative scenario is consistent with the nonnegligible fraction of *apo* VcINDY we estimated to be present under these experimental conditions. Furthermore, it could explain the apparent lack of substrate dependence observed relative to our smFRET experiments in Buffer LX (*SI Appendix*, Fig. S9). This cooperative cosubstrate-binding scenario agrees with our thermodynamic modeling (Fig. 5), which predicts that an optimized transporter that has evolved to minimize slippage cycle flux should have extremely stable *apo* and fully bound states with very weak binding of the initial cosubstrate(s) (Fig. 6). The extent of that optimization reflects how nature has navigated the speed–accuracy tradeoff between rapid transport and minimal slippage. This raises the possibility that some secondary active transporters undergo a nonnegligible amount of slippage in order to be efficient at transporting the driven cosubstrate as long as they do not significantly waste the free energy of the driving cosubstrate.

Experimental evidence is also consistent with a cooperative cosubstrate-binding mechanism. For instance, our X-ray crystallographic structures show that Na1, Na2, and dicarboxylate substrates all interact with common hairpin loop elements (Fig. 7). That the conformation of VcINDY is effectively independent of dicarboxylate identity suggests that this fully bound conformation is very stable—as predicted in our modeling of optimal cosubstrate binding. Moreover, recent experiments demonstrated that in the presence of high concentrations of only Na^+, cysteine residues engineered near the substrate-binding pocket of VcINDY are protected from modification by maleimide-derivatized polyethylene glycol (11, 16) indicating some interaction between Na^+ and the *apo* VcINDY binding pocket. This result is consistent with a Na^+-first binding order and with predictions that slippage is minimized and that transport is optimized by weak binding of the first cosubstrate(s) (Fig. 6). In future work, determination of the affinities and binding order of cosubstrates, together with structure characterization of the sites, will be required to develop a comprehensive understanding of how cosubstrate binding is employed as a mechanism to avoid slippage cycles during vectorial transport by VcINDY.

Conclusion

Previous studies of the structure, transport biochemistry, and alternating access mechanism of VcINDY have established it as a prototypical membrane-bound transporter of the DASS family (8–11, 13, 14, 17). Here, we have advanced this fundamental understanding of the DASS family and secondary active transport by directly determining how the conformational dynamics of VcINDY enable it to achieve alternating access and how those dynamic motions are tuned in order to maintain the efficiency of the transport cycle. Specifically, our study provides direct evidence that i) the VcINDY translocation reaction uses a thermally driven, elevator mechanism; ii) the rate of elevator conformational changes is an order of magnitude faster than the substrate transport turnover rate; iii) VcINDY protomer conformational dynamics are noncooperative; iv) the VcINDY transport cycle uses cooperative substrate binding to minimize slippage; and v) cooperative substrate binding is a general approach to optimize transport efficiency for certain secondary active transporters. Altogether, these findings immediately suggest future studies aimed at determining the extent to which highly cooperative cosubstrate binding and/or additional conformational dynamics that gate transport (1, 4, 36) enable VcINDY to avoid slippage cycles during vectorial transport. Overall, the powerful smFRET-based experimental modality for interrogating the function and regulation of VcINDY established here is easily extended to study the transport cycles of other DASS family transporters, and even dimeric transporters from other families, to further our understanding of secondary active transport.

Materials and Methods

Expression and Purification of VcINDY. Expression and purification of wild type VcINDY was carried out according to our previous protocol (13). Briefly, *Escherichia coli* BL21-AI cells (Invitrogen) were transformed with a modified pET vector encoding N-terminal 10× His tagged VcINDY. Cells were grown for 16 h postinduction at 19 °C. After cell breakage, membranes were solubilized in 1.2% N-decyl-β-maltoside (DM) and the protein was purified on a Ni-NTA affinity column (Qiagen). Following His-tag removal, VcINDY was further purified by size-exclusion chromatography (SEC) in buffer containing 25 mM Tris pH 8, 100 mM NaCl, 5% glycerol, 0.1% DM unless otherwise indicated.

Purification of VcINDY Mutants. Expression and purification of VcINDY mutants G211C and S436C was performed as with the wildtype protein, but with the following modifications. All buffers contained 10 mM sodium citrate but not glycerol. Membranes were solubilized in 1.0% N-dodecyl-β-maltoside (DDM). The protein was eluted from Ni-NTA agarose beads using 300 mM imidazole. Finally, the SEC buffer contained 25 mM Tris pH 8, 100 mM NaCl, 0.1% DDM, and 0.5 mM TCEP.

Expression, Purification, and Biotinylation of Membrane Scaffolding Protein. Expression and purification of membrane scaffolding protein (MSP1E3D1) was carried out according to a previously published protocol (37). In brief, *E. coli* BL21-Gold (DE3) cells (Agilent) were transformed with a modified pET28a vector encoding N-terminal 7× His tagged MSP with a mutated cysteine at position 277 for biotinylation. Cells were grown at 30 °C for 4 h post 0.1 mM

IPTG induction at OD 0.8. After cell breakage, lysate was bound to Ni-NTA agarose beads (Qiagen) for 4 h with nutation at 4 °C. Protein was eluted with 100 to 250 mM imidazole and dialyzed into 100 mM Tris pH 7.4, 300 mM NaCl for 1 h at 4 °C. The His-tag was then removed by overnight TEV digestion at 12 °C. Cleaved MSP protein was subsequently biotinylated using EZ-Link Maleimide-PEG11-Biotin (Promega) according to the manufacturer's instructions. Specifically, a 20-fold molar excess of biotin reagent dissolved in DMSO was incubated with protein overnight at 4 °C. Labeled MSP1E3D1-T277C protein was further purified by SEC in 100 mM NaCl, 1 mM TCEP, 20 mM Tris pH 7.4.

Fluorophore Labeling. Stock solutions of Alexa Fluor 555 C2 maleimide (AF555) and Alexa Fluor 647 C2 maleimide (AF647) were prepared in anhydrous DMSO at 3 mM and stored at −20 °C. Prior to labeling, a 1 mg/mL solution of VcINDY (total of 0.5 mg to 1 mg) was treated with 10 mM DTT for 2 h at 4 °C to reduce the cysteines. DTT was then removed by three serial dilutions in SEC buffer (25 mM tris pH 8.0, 100 mM NaCl, 5% glycerol, 0.15% DDM, 1 mM TCEP) followed by reconcentration with an Amicon concentrator (cutoff 50 kDa). This preparation was incubated with a 10-fold molar excess of AF555 and AF647 overnight at 4 °C, protected from light. The resulting solution was purified on Superdex 200 10/300 GL size exclusion column to remove the unreacted dye. Fractions from the elution peak were combined and the labeling stoichiometry was determined with a spectrophotometer using the following wavelengths and extinction coefficients: VcINDY: $\lambda = 280$ nm with $\epsilon = 57{,}075$ $\mathrm{cm}^{-1}\mathrm{M}^{-1}$; AF555: $\lambda = 556$ nm with $\epsilon = 155{,}000$ cm^{-1} M^{-1}; AF647: $\lambda = 651$ nm with $\epsilon = 270{,}000$ cm^{-1} M^{-1}. Typical labeling efficiency was 42% for each dye.

Nanodisc Reconstitution. A thin film of *E. coli* polar lipid (EPL) was prepared by adding 10 mg of chloroform stock solution to a glass test tube. The solvent was evaporated with argon gas and the test tube was placed in a vacuum chamber at ~1 mTorr for ~2 h. This lipid film was resuspended by adding 285 µL of nanodisc buffer (20 mM Tris pH7.4; 100 mM NaCl, 0.5 mM EDTA, 0.5 mM TCEP) followed by vortexing and sonication in an ultrasonic bath (Laboratory Supplies Co. Inc, Model G112SP1T) with 10 s bursts alternating with 10 s rests for a total of 3 min. This aqueous lipid solution was solubilized by adding 215 µL of 10% DDM to produce 500 µL of final lipid stock concentration at 20 mg/mL.

To reconstitute VcINDY into nanodiscs, detergent-solubilized EPL was added to VcINDY at a molar ratio of 280 and incubated on ice for 10 min. Biotinylated MSP was then added to this mixture at an eightfold molar excess to produce 500 µL of a solution containing 2.5 mM EPL, 72 µM MSP, 9 µM VcINDY, and 7.2 mM DDM. This solution was incubated at 4 °C for 1 h followed by the addition of SM-2 Bio-Beads in three steps: 300 mg initially, 200 mg added 60 min later, and 100 mg added at 90 min later and incubated overnight. During these incubations, solutions were kept at 4 °C and gently stirred.

Nanodiscs containing VcINDY were purified by incubating the solution with 0.5 mL of Ni-NTA beads pre-equilibrated with nanodisc buffer (20 mM Tris pH = 7.4; 100 mM NaCl; 0.5 mM EDTA; 0.5 mM TCEP) for 30 min at 4 °C. The beads were packed into a column and washed with 1 mL of nanodisc buffer. Nanodiscs containing VcINDY were then eluted with 2 ml nanodisc buffer supplemented with 0.3 M imidazole and the peak elution fractions were pooled and concentrated with an Amicon concentrator (cutoff 50 kDa). The concentrated sample was fractionated on Superdex 200 10/300 GL size exclusion column (GE Healthcare) pre-equilibrated and eluted with nanodisc buffer. The fractions were evaluated by SDS-PAGE and those containing both MSP and VcINDY were pooled, and concentrated to ~0.2 to 0.4 mg/mL. Typical yield for 1 mg of VcINDY was ~0.4 mg of reconstituted protein (VcINDY plus MSP). Electron microscopy grids were prepared in 2% (w/v) phosphotungstic acid (pH 7.5) and were examined in a Talos L120C transmission electron microscope (FEI-Thermo Fisher Scientific). Nanodisc samples were frozen in aliquots and stored at −80 °C.

Proteoliposome Reconstitution and Transport Assay. VcINDY was reconstituted into proteoliposomes as previously described (8, 10). These proteoliposomes were then used in succinate transport assays as previously described except at room temperature (8, 10). Briefly, proteoliposomes were exchanged into external buffer containing tritiated succinate with an inward-facing Na^+ gradient, samples taken at various time points were quenched and rapidly filtered over a 0.22 µm nitrocellulose membrane, and then succinate content inside the proteoliposomes was measured using scintillation counting. Transport rates were calculated from a linear fit to at least three data points within the first minute of the transport reaction.

Crystallization of Wild-Type VcINDY with Substrates. Crystals of VcINDY were grown with a protein concentration of 6 mg/mL at 4 °C in hanging-drop vapor diffusion. For VcINDY-succinate, crystallization was carried out with 30% PEG 300, 5 mM sodium succinate, 200 mM sodium chloride, and 100 mM MES pH 5.8. VcINDY-fumarate crystals were grown with 37.5% PEG 300, 200 µM sodium fumarate, and 100 mM sodium acetate pH 4.6. For VcINDY-malate, crystals were grown with 25% PEG 400, 20 mM sodium malate, and 100 mM sodium acetate pH 5.0.

TIRF Microscopy. smFRET imaging experiments were performed on a prism-based, wide-field TIRF microscope at a temperature of 21 ± 1 °C. Briefly, a 532 nm diode-pumped solid-state continuous-wave laser (Laser Quantum, GEM532) was directed through an acousto-optic modulator (AOM) (Isomet, IMDD-P80L) such that the +1 order peak is directed toward a prism suspended over a 60×, 1.2 NA water immersion objective (Nikon). VcINDY embedded nanodiscs were tethered to the surface of quartz slides derivatized with dilute biotin-poly(ethylene)-glycol (PEG) in PEG via a biotin–streptavidin–biotin bridge, and illuminated with the TIR field generated at the slide/buffer interface. The instantaneous illumination power incident at the prism entry face was 40 mW (estimated density of 4.3 $\mathrm{W/cm}^2$), and the AOM was modulated with a 50% duty cycle at 1 MHz, such that the time averaged power was 20 mW. Fluorescence was collected through the objective, separated with a multiwavelength imager (Photometrics, Dual-view), and imaged onto a water-cooled electron-multiplying charge coupled device (Andor, iXon Ultra 888). Movies were collected for 2,000 frames at 25 ms exposures with 2× binning, 600 EM gain, 1× pre-amp gain, 30.0 MHz readout mode, 0.60 µs vertical speed, and +4 clock voltage running at −67 °C using the open source microscopy software Micro-Manger (38).

TIRF Microscopy Imaging Buffers. VcINDY homodimers were imaged in the following buffers, which all contained 100 mM KCl, and 20 mM Tris-Cl (pH_{25C} = 7.5). Buffer LX: 100 mM choline chloride. Buffer LS: 100 mM choline chloride, and 1 mM succinic acid. Buffer HX: 100 mM NaCl. Buffer HS: 100 mM NaCl, and 1 mM succinic acid. All buffers also contained 1% β-D-glucose, 1 mM trolox, 0.0025 U glucose oxidase, 0.02 U catalase, 1 mM 1,3,5,7-cyclooctatetraene, and 1 mM 3-nitrobenzyl alcohol as photostabilizing additives.

TIRF Microscopy Data Analysis. Diffraction-limited spots of fluorescence intensity within the first 400 frames (10 s) were located in both the donor and acceptor fluorescence channels. Intensity versus time trajectories were estimated using the iterative, maximum likelihood formulas for intensity estimation $N = (\Sigma_{xy}(d_{xy}-b)\Psi_{xy})/(\Sigma_{xy}\Psi^2_{xy})$ and $b = (\Sigma_{xy}(d_{xy}-N\Psi_{xy}))/(\Sigma_{xy}1)$, where (x,y) is a pixel location, N is the fluorescence intensity, b is the background intensity, and Ψ is a fixed width, Gaussian-shaped point spread function with width defined by the TIRF microscope optics (39). Donor and acceptor fluorescence channels were aligned using a 4th order polynomial transform of ~2,800 control points obtained from an image of an array of subdiffraction limit nanopatterned features localized in both channels. Trajectories were manually classified to select trajectories from only donor–acceptor labeled molecules (*SI Appendix*, Fig. S1). The photobleaching point for each E_{FRET} trajectory was inferred using Bayesian inference (*SI Appendix*). A nonlinear filter (40) was applied to fluorescence intensity trajectories for easier visualization in intensity and E_{FRET} trajectory plots, but all analyses (e.g., generation of histograms, kinetic modeling, etc.) were performed using the unfiltered data.

Kinetic Modeling of smFRET Data. Optimal kinetic models were obtained by estimating a global HMM from all of the E_{FRET} trajectories for a single experimental condition using variational Bayesian inference as implemented in the tMAVEN software (25, 26) (*SI Appendix*, Fig. S6). Specifically, a variational posterior with separable emissions and kinetics was optimized using the expectation–maximization algorithm until the logarithm of the evidence lower bound (ELBO) converged to a relative change threshold of 10^{-10}. For each collection of E_{FRET} trajectories, model selection was performed by estimating separate HMMs with one through ten states, and then selecting the HMM with the largest ELBO (*SI Appendix*, Fig. S8) as the optimal kinetic model.

Data, Materials, and Software Availability. Mutant VcINDY and MSP expression vectors are available upon request. VcINDY structures with fumarate, malate, and succinate bound were deposited in the Protein Data Bank with IDs 6OKZ (41), 6OL0 (42), and 6OL1 (43), respectively. Code to process TIRF microscopy movies, which are available upon request due to size, was previously published (39), and code to analyze smFRET data and kinetics is available in the tMAVEN software (25).

ACKNOWLEDGMENTS. R.L.G. acknowledges support from the NIH through grants R01-GM084288, R01-GM137608, and R35-GM153724. D.-N.W. acknowledges support from the NIH through grants R01-GM121994, R01-NS108151, and R01-DK099023, the G. Harold and Leila Y. Mathers Foundation, and the TESS Research Foundation. C.M. and J.A.M. acknowledge support from the National Institute of Neurological Disorders and Stroke Intramural Program, and C.M. acknowledges support from the Biotechnology and Biological Sciences Research Council through grant BB/V007424/1. D.L.S. acknowledges support from NIH through grant R35-GM144109. J.F.H. acknowledges support from NIH through grants R01-GM127883. E.T. acknowledges support from NIH through grants P41-GM104601 and R01-GM123455. R.L.G., D.-N.W., and E.T. acknowledge support from the NIH through grant R01-DK135088. D.B.S. acknowledges support, in part, from an American Cancer Society Postdoctoral Fellowship (PF-17-135-01) and from the Office of the Assistant Secretary of Defense for Health Affairs, through the Peer Reviewed Cancer Research Program under Award No. W81XH-16-1-0153. Crystal screening and X-ray data collection were carried out at NSLS-II Brookhaven National Laboratory and at Argonne National Laboratory, Structural Biology Center (SBC) at the Advanced Photon Source. SBC-CAT is operated by Univ. Chicago Argonne, LLC, for the US Department of Energy, Office of Biological and Environmental Research under contract DE-AC02-06CH11357. Electron microscopy was performed at the NYU School of Medicine Microscopy Core. We thank the staff at the Columbia Precision Biomolecular Characterization Facility for access to molecular biology and biophysical instrumentation.

Author affiliations: [a]Department of Chemistry, Columbia University, New York, NY 10027; [b]Department of Cell Biology, New York University School of Medicine, New York, NY 10016; [c]Division of Natural Sciences, School of Biosciences, University of Kent, Canterbury, Kent CT2 7NH, United Kingdom; [d]Department of Biochemistry, Theoretical and Computational Biophysics Group, NIH Center for Macromolecular Modeling and Bioinformatics, Beckman Institute for Advanced Science and Technology, Center for Biophysics and Quantitative Biology, University of Illinois at Urbana-Champaign, Urbana, IL 61801; [e]Department of Biological Sciences, Columbia University, New York, NY 10027; [f]Membrane Transport Biophysics Section, Porter Neuroscience Research Center, National Institute of Neurological Disorders and Stroke, NIH, Bethesda, MD 20892; and [g]Department of Physiology & Cellular Biophysics, Columbia University Irving Medical Center, New York, NY 10032

Author contributions: C.D.K.-T., E.T., J.F.H., D.L.S., J.A.M., D.-N.W., and R.L.G. designed research; C.D.K.-T., M.L.L.-R., C.M., D.B.S., J.J.M., and J.S. performed research; C.D.K.-T., M.L.L.-R., C.M., D.B.S., J.J.M., J.S., and J.F.H. contributed new reagents/analytic tools; C.D.K.-T., C.M., and D.B.S. analyzed data; and C.D.K.-T., J.A.M., D.-N.W., and R.L.G. wrote the paper.

The authors declare no competing interest.

1. W. D. Stein, W. R. Lieb, *Transport and Diffusion across Cell Membranes* (Academic Press, 1986).
2. O. Jardetzky, Simple allosteric model for membrane pumps. *Nature* **211**, 969–970 (1966).
3. L. R. Forrest, R. Krämer, C. Ziegler, The structural basis of secondary active transport mechanisms. *Biochim. Biophys. Acta* **1807**, 167–188 (2011).
4. D. Drew, O. Boudker, Shared molecular mechanisms of membrane transporters. *Annu. Rev. Biochem.* **85**, 543–572 (2016).
5. D. Markovich, "Sodium-sulfate/carboxylate cotransporters (SLC13)" in *Current Topics in Membranes*, M. O. Beven, Ed. (Elsevier, 2012), vol. 70, pp. 239–256.
6. M. J. Bergeron, B. Clémençon, M. A. Hediger, D. Markovich, SLC13 family of Na^+-coupled di- and tri-carboxylate/sulfate transporters. *Mol. Aspects Med.* **34**, 299–312 (2013).
7. D. B. Sauer *et al.*, The ups and downs of elevator-type di-/tricarboxylate membrane transporters. *FEBS J.* **289**, 1515–1523 (2022).
8. C. Mulligan, G. A. Fitzgerald, D.-N. Wang, J. A. Mindell, Functional characterization of a Na^+-dependent dicarboxylate transporter from *Vibrio cholerae*. *J. Gen. Physiol.* **143**, 745–759 (2014).
9. G. A. Fitzgerald, C. Mulligan, J. A. Mindell, A general method for determining secondary active transporter substrate stoichiometry. *Elife* **6**, e21016 (2017).
10. C. Mulligan *et al.*, The bacterial dicarboxylate transporter VcINDY uses a two-domain elevator-type mechanism. *Nat. Struct. Mol. Biol.* **23**, 256–263 (2016).
11. C. D. D. Sampson, M. J. Stewart, J. A. Mindell, C. Mulligan, Solvent accessibility changes in a Na^+-dependent C4-dicarboxylate transporter suggest differential substrate effects in a multistep mechanism. *J. Biol. Chem.* **295**, 18524–18538 (2020).
12. C. D. D. Sampson, C. Fàbregas Bellavista, M. J. Stewart, C. Mulligan, Thermostability-based binding assays reveal complex interplay of cation, substrate and lipid binding in the bacterial DASS transporter, *Vc*INDY. *Biochem. J.* **478**, 3847–3867 (2021).
13. R. Mancusso, G. G. Gregorio, Q. Liu, D.-N. Wang, Structure and mechanism of a bacterial sodium-dependent dicarboxylate transporter. *Nature* **491**, 1–6 (2012).
14. R. Nie, S. Stark, J. Symersky, R. S. Kaplan, M. Lu, Structure and function of the divalent anion/Na+ symporter from *Vibrio cholerae* and a humanized variant. *Nat. Commun.* **8**, 15009 (2017).
15. D. B. Sauer *et al.*, Structure and inhibition mechanism of the human citrate transporter NaCT. *Nature* **591**, 157–161 (2021).
16. D. B. Sauer *et al.*, Structural basis of ion – substrate coupling in the Na+-dependent dicarboxylate transporter VcINDY. *Nat. Commun.* **13**, 2644 (2022).
17. D. B. Sauer *et al.*, Structural basis for the reaction cycle of DASS dicarboxylate transporters. *Elife* **9**, e61350 (2020).
18. Y. Li *et al.*, Substrate translocation and inhibition in human dicarboxylate transporter NaDC3. *Nat. Struct. Mol. Biol.* **32**, 502–512 (2025).
19. T. J. Lambert, FPbase: A community-editable fluorescent protein database. *Nat. Methods* **16**, 277–278 (2019).
20. I. G. Denisov, S. G. Sligar, Nanodiscs in membrane biochemistry and biophysics. *Chem. Rev.* **117**, 4669–4713 (2017).
21. T. H. Bayburt, S. G. Sligar, Membrane protein assembly into nanodiscs. *FEBS Lett.* **584**, 1721–1727 (2010).
22. D. Wöhlert, M. J. Grötzinger, W. Kühlbrandt, Ö. Yildiz, Mechanism of Na+-dependent citrate transport from the structure of an asymmetrical CitS dimer. *Elife* **4**, e09375 (2015).
23. J. W. Kim *et al.*, Structural insights into the elevator-like mechanism of the sodium / citrate symporter CitS. *Sci. Rep.* **7**, 2548 (2017).
24. J. S. Lolkema, D. J. Slotboom, Structure and elevator mechanism of the Na+-citrate transporter CitS. *Curr. Opin. Struct. Biol.* **45**, 1–9 (2017).
25. A. R. Verma, K. K. Ray, M. Bodick, C. D. Kinz-Thompson, R. L. Gonzalez, Increasing the accuracy of single-molecule data analysis using tMAVEN. *Biophys. J.* **123**, 2765–2780 (2024).
26. C. D. Kinz-Thompson, K. K. Ray, R. L. Gonzalez, Bayesian inference: The comprehensive approach to analyzing single-molecule experiments. *Annu. Rev. Biophys.* **50**, 191–208 (2021).
27. D. Montepietra *et al.*, FRETpredict: A Python package for FRET efficiency predictions using rotamer libraries. *Commun. Biol.* **7**, 1–10 (2024).
28. T. L. Hill, *Free Energy Transduction and Biochemical Cycle Kinetics* (Dover Publications, 2005).
29. A. Fersht, *Structure and Mechanism in Protein Science: A Guide to Enzyme Catalysis and Protein Folding* (World Scientific, 2017).
30. C.-J. Lo, M. C. Leake, R. M. Berry, Fluorescence measurement of intracellular sodium concentration in single *Escherichia coli* cells. *Biophys. J.* **90**, 357–365 (2006).
31. S. Maity *et al.*, High-speed atomic force microscopy reveals a three-state elevator mechanism in the citrate transporter CitS. *Proc. Natl. Acad. Sci. U.S.A.* **119**, e2113927119 (2022).
32. N. Akyuz, R. B. Altman, S. C. Blanchard, O. Boudker, Transport dynamics in a glutamate transporter homologue. *Nature* **502**, 114–118 (2013).
33. G. B. Erkens, I. Hänelt, J. M. H. Goudsmits, D. J. Slotboom, A. M. van Oijen, Unsynchronised subunit motion in single trimeric sodium-coupled aspartate transporters. *Nature* **502**, 119–123 (2013).
34. Y. Ruan *et al.*, Direct visualization of glutamate transporter elevator mechanism by high-speed AFM. *Proc. Natl. Acad. Sci. U.S.A.* **114**, 1584–1588 (2017).
35. A. A. Garaeva, D. J. Slotboom, Elevator-type mechanisms of membrane transport. *Biochem. Soc. Trans.* **48**, 1227–1241 (2020).
36. J. S. Lolkema, D. J. Slotboom, Models to determine the kinetic mechanisms of ion-coupled transporters. *J. Gen. Physiol.* **151**, 369–380 (2019).
37. I. G. Denisov, Y. V. Grinkova, A. A. Lazarides, S. G. Sligar, Directed self-assembly of monodisperse phospholipid bilayer nanodiscs with controlled size. *J. Am. Chem. Soc.* **126**, 3477–3487 (2004).
38. A. D. Edelstein *et al.*, Advanced methods of microscope control using μManager software. *J. Biol. Methods* **1**, 10 (2014).
39. K. K. Ray *et al.*, Entropic control of the free-energy landscape of an archetypal biomolecular machine. *Proc. Natl. Acad. Sci. U.S.A.* **120**, e2220591120 (2023).
40. G. Haran, Noise reduction in single-molecule fluorescence trajectories of folding proteins. *Chem. Phys.* **307**, 137–145 (2004).
41. D. B. Sauer *et al.*, Structure of VcINDY bound to Fumarate. Protein Data Bank. https://www.rcsb.org/structure/6OKZ. Deposited 15 April 2019.
42. D. B. Sauer *et al.*, Structure of VcINDY bound to Malate. Protein Data Bank. https://www.rcsb.org/structure/6OL0. Deposited 15 April 2019.
43. D. B. Sauer *et al.*, Structure of VcINDY in complex with Succinate. Protein Data Bank. https://www.rcsb.org/structure/6OL1. Deposited 15 April 2019.